CHAPTER 7

Dual-Modality Imaging

A. Lahooti*, S. Shanehsazzadeh†, S. Laurent†,‡
*Tehran University of Medical Science, Tehran, Iran
†University of Mons, Mons, Belgium
‡Center for Microscopy and Molecular Imaging (CMMI), Gosselies, Belgium

7.1 THE NECESSITY OF DUAL MODALITY IMAGING

The desired goal in clinical diagnosis is the early detection of a disease at the vascular, cellular, or genomic level rather than at the systematic or symptomatic level, in order to positively influence the course of the disease. Noninvasive functional and morphological imaging increases the chances of accomplishing this aim [1].

The enormous development of image fusion techniques (mixing two or sometimes three different images from different devices such as computed tomography (CT), magnetic resonance imaging (MRI), single-photon emission computed tomography (SPECT), positron emission tomography (PET), ultrasound (US), and optical imaging (OI)) over the past 20 years has shown that the fusion of images from complementary modalities offers a more complete and accurate assessment of disease than do images from a single modality [2]. Image registration and image fusion techniques have been successful in fusing images of the brain from different modalities, but they have achieved rather limited success for other parts of the body. The combination of CT and PET was introduced commercially in 2001, followed by CT and SPECT in 2004, and simultaneously PET/MRI [2,3]. However, the idea of combining PET and MRI imaging devices in a single system was first recommended in the early mid-1990s by Hammer and Hammer et al. [4,5]. As we will discuss briefly in the following sections of this chapter, each imaging modalities have their own merits and limitations and disadvantages, and in order to overcome these limitations, a combination of two or three modalities may provide better results with less limitations. Using dual modalities not only is because of overcoming the limitation of each modality but also could be the best way to manipulate the whole capabilities of the contrast agents and to defeat their physical restrictions.

In each imaging modality and in order to have a better contrast, we have to use specific agents. In the United States, we can use microbubbles [6] or in

Iron Oxide Nanoparticles for Biomedical Applications
https://doi.org/10.1016/B978-0-08-101925-2.00006-1
© 2018 Elsevier Ltd.
All rights reserved.

CT, we used bromide and iodine complexes or tantalum, tungsten, and bismuth enteric [7,8], whereas in SPECT and PET, we need gamma emitter radioisotopes (^{111}In, ^{67}Ga, and ^{99m}Tc) [9–11] and positron emitter radioisotopes such as ^{61}Cu, ^{64}Cu, ^{68}Ga, and ^{18}F [12–15]. In targeted imaging nuclear medicine, there is always a possibility that the biomarker detached from the radioisotope and what we see is the radioisotope alone and not the radiolabeled biomarker; therefore, it is necessary to have or to compare the images (or the biodistribution pattern) of patients or rodents after injection of free radioisotopes [12,16]. On the other hand, we may have the same problem in MR molecular imaging; as you know, we have two types of contrast agents in MRI: one is paramagnetic agents such as Gd^{3+} (gadolinium (III) chelates) compounds or Mn^{2+} that are known as positive contrast agents and increase the signal intensity [17,18]. As shown in Fig. 7.1, the signal intensity in the uptake area is increased when we used positive contrast agents.

This brightness in the images can be also because of the fat or the bone (it depends on the image parameters in MRI such as echo time and repetition time that are known as TE and TR, respectively) as shown in Fig. 7.1. Therefore, in MRI, we always should compare or sometimes subtracts preinjection images from postinjection images as it happens in MRI angiography. We have the same challenge for negative contrast agents such as iron

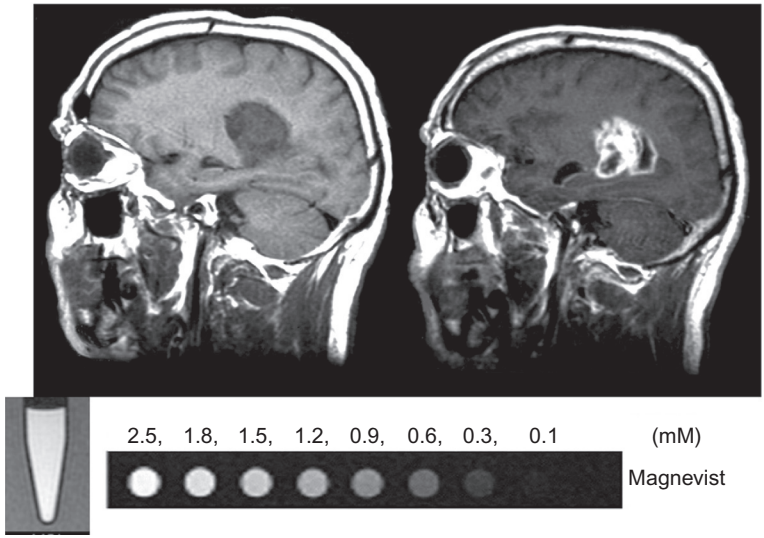

Fig. 7.1 Upper image: MR-T_1 images of a glioblastoma patient before and after Gd injection. Notice the contrast enhancement due to the large magnetic moment of Gd (available in http://home.physics.wisc.edu/gilbert/radio.htm). Down: different concentrations of Magnevist as common MRI contrast agents.

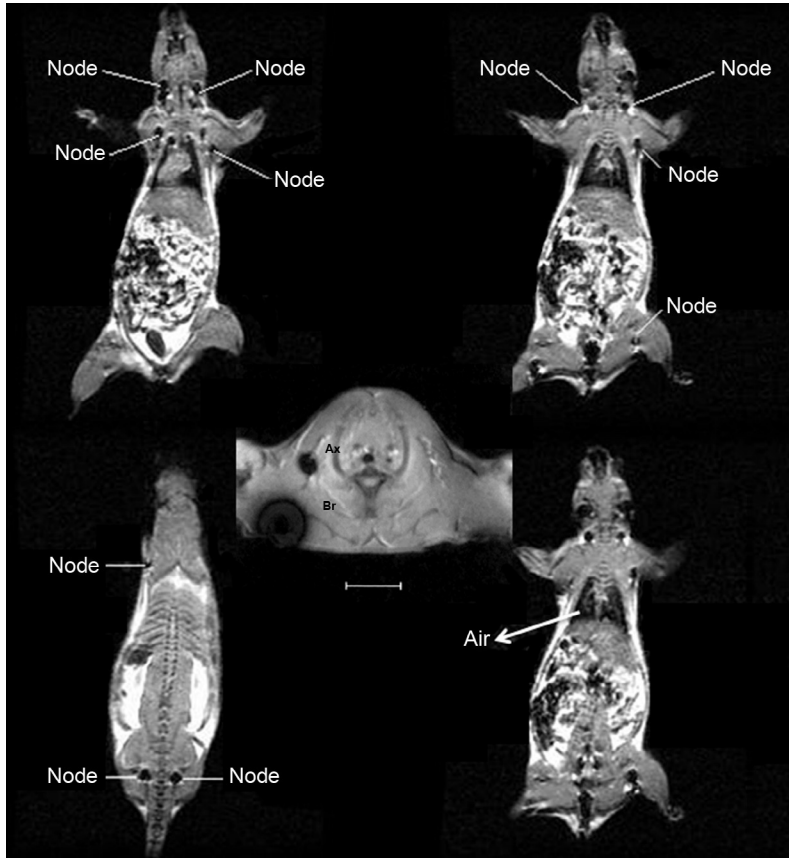

Fig. 7.2 Different images of superparamagnetic iron oxide nanoparticles (SPION) after injection intravenously. As clearly indicated, the SPIONS and air can simply misunderstand in T_2-weighted images.

oxide nanoparticles that produce dark spots in the MR images as demonstrated in Fig. 7.2.

Therefore, using dual-modality contrast agents not only integrates the benefit of both modalities but also can verify what we see in the both probes together and not the specific agents that were detached from the biomarker (free radioisotopes or free iron oxide).

7.2 MOLECULAR IMAGING

Currently, most of the clinicians are trying to reach a successful targeted and personalized treatment, believing that molecular imaging plays a very crucial

role in achieving this aim. The biological targets, understanding its complexities for diagnosis, and treatment of the disease are visualized using it [19–21]. As the Society of Nuclear Medicine has described, molecular imaging can lead to the visualization, characterization, and measurement of biological processes at the molecular and cellular levels in humans and other living systems; therefore, imaging of biological targets results in early detection of various diseases effectively [22]. Each of the mentioned modalities (CT, MRI, SPECT, PET, US, and optical imaging (OI)) has its own pros and cons. Fig. 7.3 shows briefly a comparison between SPECT or PET and MRI.

In order to obtain all the required information about the biological processes and function of an organ, we need to combine two or more modalities for using the advantages of them and weakening the disadvantages. This approach causes a better reliability of the images [19]. Table 7.1 describes the different types of devices used in molecular imaging and expresses their advantages and disadvantages. Also, it mentions briefly some current probes utilized in that imaging device.

7.3 MULTIMODALITY IMAGING

Concerning the advantages and disadvantages of imaging modalities for the combination of anatomical, functional, and molecular information,

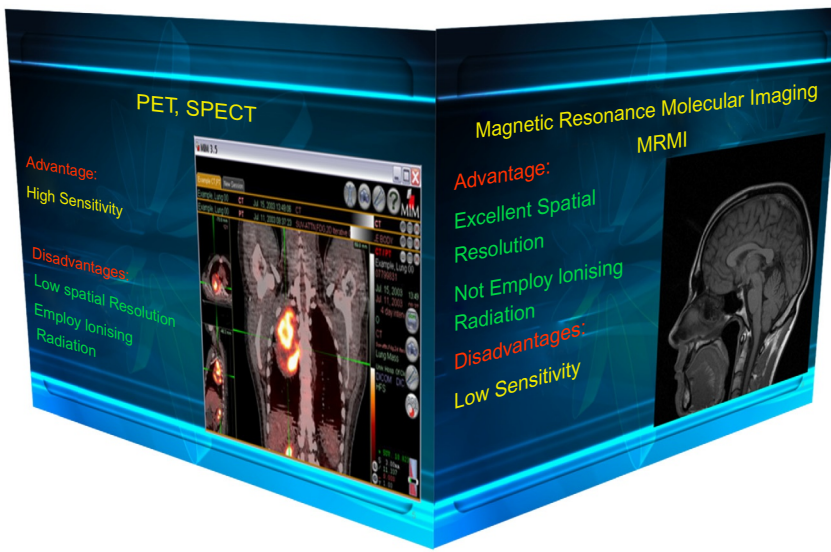

Fig. 7.3 On the left, a picture of PET/MRI and the positive and negative points of PET and SPECT devices and, on the right, MR image and its positive and negative points.

Table 7.1 Molecular imaging system and their advantages and disadvantages

Device	Probes	Advantage	Disadvantages	Ref.
Computed tomography (CT)	High atomic number elements such as bromide and iodine complex, iodinated nanoparticles, gold nanoparticles, alkaline earth-based nanoparticles	Best clinical spatial resolution (0.5–1 mm), no limitation in depth, good temporal resolution, clinical utility, widely available, relatively cost-effective, highly efficient	Poor sensitivity (requires large mass of imaging agents), ionizing radiation, limited soft tissue resolution, limited molecular imaging applications	[8,23–25]
Ultrasound systems	Microbubbles	Low cost, portable, safe (the lack of ionizing radiation), high frame rate (widely available real-time imaging modality (200 f/s)), and has a better depth of penetration than optical imaging, the spatial resolution about 0.01–0.1 mm for superficial (few mm depth) applications and 1–2 mm for deeper (few cm depth) applications, flow information, good temporal resolution, quantitative data, real-time practice, noninvasiveness, relatively inexpensive cost	Low numbers of retained contrast agents, high background from freely circulating agents(waiting period), limited field of view, the lack of quantitative ability, possible immune responses, low sensitivity (at least 10^7 bubbles needed)	[23,26,27]

Continued

Table 7.1 Molecular imaging system and their advantages and disadvantages—cont'd

Device	Probes	Advantage	Disadvantages	Ref.
Optical imaging and optical bioluminescence	Fluorophore, fluorescent protein, luciferin, quantum dot, etc.	Safe (nonionizing), high sensitivity, low cost, portable, vascular and intravascular signals, high temporal sensitivity	Low depth resolution <1 cm, poor spatial resolution, surface-weighted imaging, autofluorescence, tomography challenges	[23,28]
MRI	Gadolinium complexes, Dotarem, Gadovist, iron oxide nanoparticles (USPIO, SPION), manganese complexes, cobalt nanoparticles,	No limitation in depth, high spatial resolution, safe, good soft tissue contrast, provides both anatomical and functional information	Low sensitivity(10^{-5} M), relatively long acquisition time, no direct quantitative data, requires expensive equipment	[23,29,30]
SPECT	Most of the radionuclides that emitted gamma rays (^{99m}Tc, ^{67}Ga, ^{111}In, ^{123}I)	No limitation in depth, high sensitivity and quantifiability, potential to detect multiple probes simultaneously in contrast to PET (cocktail therapy or using two or more radionuclides simultaneously)	Low spatial resolution (8–10 mm clinical), lower sensitivity than pet (10^{-11} M), the lack of anatomical parameters	[23,29]
PET	Radionuclides that emitted positrons (^{68}Ga, ^{76}Br, ^{94m}Tc, ^{11}C, ^{13}N, ^{15}O, ^{18}F, ^{64}Cu)	No limitation in depth, high sensitivity and quantifiability (10^{-12} M), metabolic imaging, better spatial resolution than SPECT (5–7 mm)	The lack of anatomical parameters, requires specialized equipment, requires radionucleotide facilities, requires expensive equipment	[23,29,30]

PET/CT	Au nanoparticles labeled with positron emitters	Better attenuation correction, time of flight, relatively cheaper than PET/MRI and variable, relatively faster techniques than PET/MRI, advantages to detect corticallesions, lung lesions and lymph nodes (PET/CT superior to PET/MRI)	Higher absorbed dose compare with PET/MRI, lower soft tissue contrasts, reduced sensitivity of detection of metastases in organs with high glucose uptake such as the brain	[31–35]
PET/MRI	Magnetic nanoparticles labeled with positron emitters	Higher soft tissue contrast, reduced radiation exposure, advanced MRI techniques such as perfusion imaging, diffusion imaging, and MR spectroscopy. It is superior than PET/CT for the patients who need multiple follow-up examinations because of lower radiation dose (75% reduction in dose); PET/MRI showed superior lesion detectability compared with PET/CT	Had halo artifact, needs higher technology, needs more time for reconstructions and attenuation correction calculation, challenging due to the presence of magnetic field (needs avalanche photodiode (APD)), increased eddy currents and heating, the highest costs (5 million euros)	[31,32,35–38]

multimodality imaging was suggested. In this method, images from different modalities taken at the same point are combined for using of the strengths of different modalities and yield a hybrid imaging platform with characteristics superior to those of any of its constituents considered alone. In fact, utilization of the high-resolution information coming from an anatomical or functional image in order to improve the imaging performance of the low-resolution modality is the most important feature. Moreover, the combination of anatomical and functional data by multimodal techniques, enhancement of contrast in molecular imaging, and therefore increasing of diagnostic capabilities is another benefit [39].

In the first time, the images of different modalities have been acquired separately and then merged. But because of the different positions of the patient in the two modalities and also inaccurate coregistration due to movement, the simultaneous acquisition of images was suggested. Therefore nowadays, the images get together and then fused. For PET/MRI, there are three different ways to get the images.

In the clinic, the physicians may benefit from not only anatomical images but also physiological (functional) data from single images. Besides that, since some contrast agents (CAs) in MRI are negative contrast by using dual modalities, the physicians may assure about the existence of the probe.

Furthermore, using and development of dual-modality contrast agents in some cases such as manipulation of nanoagents will increase the tumor uptakes and tumor retention due to the faiths of nanoagents.

7.4 PET/MRI

The combining of PET and MRI was presented as an idea even before PET/CT [40]. Because the primary PET/MRI systems consisted of PET and MRI elements individually that connected by a table, there were some limitations such as misregistration due to temporal separation of their data acquisition and the need of a large room for placing them [41]. For removing these problems, the fully integrated PET/MRI was designed. The main goal of development of this dual-modality imaging system was benefiting of the high anatomical spatial resolution and good soft tissue contrast of MRI and the unparalleled sensitivity and noninvasive functional molecular imaging of PET [22,42,43]. The other advantage of this hybridization was shorter scan time [41,44].

7.5 ADVANTAGES

An integrated PET/MRI may have some benefits over PET/CT imaging from a scientific and clinical approach:

(1) Real-time image acquisition enables temporal coregistration of dynamic PET data acquisition and anatomical/functional MRI data [45]. MRI can provide a range of functional information, for example, perfusion (microvessel density, vessel leakage, etc.), diffusion (cell density, microstructure, etc.), and metabolism (cell death, proliferation, etc.) [46,47].

(2) The greater contrast of MRI soft tissue, even without the use of contrast agents, allows enhanced anatomical visualization of soft tissue structures and bone marrow than CT. Therefore, it is beneficial for a number of malignant diseases, such as brain tumors; head and neck cancer; malignant melanoma; malignancies of the prostate, the cervix, and potentially the breast; liver tumors; and metastatic disease of the liver [48,49]. But for showing small lung nodules, bone, and bone structures, CT is still more sensitive than MRI [50].

Also, MRI is capable of measuring other factors that can characterize malignancies and their patient-specific biological properties [49]. These factors regularly evaluated today include blood vessels generated by a tumor and perfusion properties through dynamic contrast enhancement (DCE) imaging [51]. DCE without the rather high radiation dose in contrast with CT-based perfusion measurements can help to evaluate intravascular treatments. Another MRI method called diffusion-weighted imaging (DWI) provides information related to tumor cells and the integrity of the cellular membrane. It has the ability to determine treatment response to chemotherapy and radiation treatment [44,49,52,53].

(3) There are a lot of papers about evaluating and determining the application of PET/MRI. Some studies comparing whole-body MR with PET/CT have shown potential advantages of MRI particularly regarding the early detection of brain, liver, and bone marrow metastases [45]. For T-staging of tumors, PET/MRI is very accurate in some cancers such as head and neck cancer and primary bone and soft tissue tumors [54]. But for N-staging, the performances of MRI and PET/CT are similar. It should be mentioned that the use of new lymphotropic superparamagnetic nanoparticles can offer new opportunities for detection of

nodal micrometastases that is not possible with PET/CT [55]. For M-staging, it has been claimed that MRI may provide higher accuracy for detection of lesions, particularly in the brain, liver, and bone [55].

Furthermore, PET/MRI offers interesting opportunities for the use of dual-modality probes in both research and clinical fields [10].

In recent years, interest of hybrid imaging specially PET/MRI in cardiovascular studies is increasing. This is because of MR-based motion correction of PET images that allows improved evaluation of myocardial perfusion, providing viability information in plaque imaging and MR angiography [56].

Further interesting applications of PET/MRI are the early diagnosis of neurodegenerative disorders and dementia [57], the detection of epileptic foci [58], and the monitoring of glucose metabolism and cerebral blood flow or oxygen consumption for the investigation of focal brain ischemia [49].

(4) In fully integrated systems, MRI could also be used to provide a gating signal in addition to imaging. This is however only advantageous when MR data acquisition, MR gating data, and PET data are acquired simultaneously and for similar amounts of time; as otherwise, MR is just an expensive device to provide gating information for PET.

(5) The main advantage of MRI is a lack of ionizing radiation especially for a patient with a nononcological disease or a potentially curable oncological disease.

(6) Combined PET/MRI may decrease the imaging time; thus by reducing appointment periods, department logistics have to be improved [45,59].

7.6 CHALLENGES IN PET/MRI

The integration of PET and MRI has been an ongoing research topic for the last 20 years. Vandenberghe and Marsden, in the review paper published in 2015, discussed these challenges in details exhaustively [60]. As we stated in the beginning of this chapter, the first idea of combining PET and MRI into the single device is triggered in the mid-1990s, but after 15 years of developments, the human systems were capable of sequential simultaneously PET and MRI [61,62]. The main reason for slow progress in the development of PET/MRI is that integration of PET and MRI is much more complex than PET/CT [63]. For PET-MRI, due to the presence of magnetic fields, the

technical problem of system integration is more challenging [64]. There are different solutions for the PET/MRI system configuration. A technically relatively simple approach for PET/MRI is to place the MRI and (minimally modified) PET components in-line in a similar configuration to PET/CT (which does not allow simultaneous acquisition and will increase the acquisition times but the positive point is that it does not require the development of a completely new MRI-compatible PET system) like what Philips Company has done in the beginning (as shown in Fig. 7.4) [60,61,65]. Briefly, the main challenges in the integration of PET and MRI in a single gantry are the following:

(1) *MRI-compatible PET detectors*: One of the main challenges in totally integrated PET/MRI system is developing a PET detector compatible with MRI. Before developments in photomultiplier tubes (PMT), the conventional detectors cannot operate accurately in or even near a magnetic field specially between 0.5 and 10 T (indeed, the paths of electrons are perturbed by the magnetic field) [60]; the performance of standard PMTs is severely degraded and affected in even a weak magnetic field (about millitesla (mT) magnetic field strength) [60,66], whereas some solutions have been proposed.

- **(a)** Shielding electronics against the magnetic field for avoiding the effects of the changing gradient field and radio-frequency pulses of MRI.
- **(b)** The new generation of detectors, avalanche photodiode detectors (APD), can be used as a detector in PET instead of photomultiplier

Fig. 7.4 The primary PET/MRI imaging system from Philips Company.

tubes (PMT) [67]. Magnetic fields do not affect these new detectors [68,69]; therefore, they can be placed in MRI magnet without any degradation in performance. In addition, the potential of another type of detector entitled silicon photomultiplier (SiPM) as possible replacements in PET has been confirmed recently [6].

(2) *The gradient magnetic field in MRI* is one of the other interferences in PET system. Since the fast switching of magnetic fields can induce eddy current loops in conductive components, heating, and mechanical vibration, it must be solved, for example, by shielding electronics that was mentioned in the previous item [60].

(3) *In addition, RF interference* created by the MRI transmit coil may affect electronic components. RF shielding around PET is the effective way to decrease its effect. But unfortunately, the shielding can induce eddy currents and heating individually [60].

(4) *Space and time constraints*: Additional challenge is placing the PET detectors inside the limited space of MRI gantry that imposes other challenges to the detector technology [60]. Limited space for the PET detectors inside the MRI gantry adds another important challenge for the detector technology. In a sequential system, the PET and MRI need to be at a significant distance from each other, and therefore, the total acquisition time will be the sum of the PET acquisition time and MRI acquisition time, which leads to longer acquisition time in comparison with PET/CT scanners. Both factors (acquisition time and required installation space) are less important in small animal imaging [60].

(5) *As attenuation correction for PET* images is very vital, since one of the causes of image degradation in all nuclear medicine emission imaging techniques especially PET is variable photon attenuation in different tissues [49,60]. It should be mentioned that MR images give the information about tissue proton densities and magnetic relaxation times, not photon attenuations [45,49]. Although the attenuation correction methods proposed by combined MRI/PET systems based on segmentation methods of MR images for preparing the attenuation map totally are developed enough to use them clinically, the problem is not yet completely solved and remains an active area of research [60,70,71].

(6) *Because the PET imaging takes time usually long*, motion problem is inevitable [71]. That leads to blurring of tumors in PET images even may entirely obscure the presence of smaller lesions [70]. Also, in

the case of motion with large amplitude, it causes the severe artifacts [71]. In total, motion can be one of the sources of errors in both lesion localization and quantification [72]. Three major types of motion are the following [70]:

(a) Gross motion, head movement or subtle patient repositioning due to discomfort

(b) Periodic movement, cardiac and respiratory motion

(c) Internal shifting and distortion in the pelvic and abdominal regions

For motion solving:

(a) The first way is using high spatial resolution MR image to correct for PET motion with affectedly reduction of the spatial blurring and artifacts associated with PET movement of solid organs [71]. But inappropriately, this imaging covers a large field of view (FOV) and takes a few minutes that cause motion individually [70].

(b) Another solution is the use of external tracking devices and video cameras to record the movements for using in cardiac and respiratory gating in order to motion correction in PET/MRI [73,74].

(7) *Quantitative imaging*: In a PET/MRI system, the derivation of attenuation correction maps from either transmission imaging, emission data, or MR images is complex [75,76].

7.6.1 PET/CT or PET/MRI

There are still argues about which combination gives better results and better sensitivity or specificity, but recent studies confirm that a hybrid PET/MRI facilitates the accurate registration of metabolic and molecular aspects of the diseases with exact correlation to anatomical findings, improving the diagnostic value in identifying and characterizing of malignancies and tumor staging [77]. However, in comparison with PET/CT, PET/MRI is a relatively expensive and time-consuming examination [78], but recent studies showed that PET/MRI is comparable with PET/CT in the evaluation of colorectal cancer metastases, with a markedly higher accuracy when using combined imaging data than the modalities separately [79,80]. There are several studies that concluded that PET/MRI had superiority over the PET/CT; for example, Binse et al. in 2016 used ^{124}I for thyroid cancer and tried to compare their results between PET/CT and PET/MRI, and they concluded that PET/MRI of the neck was found

to be superior to PET/CT in detecting iodine-positive lesions. That was attributed to the higher sensitivity of the PET component [81]. In another study carried out by Sabet et al. in 2016, they tried to compare their results in detection of pancreatic cancer after injection of ^{68}Ga-DOTATOC, between PET/CT and PET/MRI images. And they found that PET/MRI was superior to PET/CT in terms of sensitivity (91% vs. 55%), negative predictive value (96% vs. 82%), and diagnostic accuracy (97% vs. 85%). ^{68}Ga-DOTATOC-PET/MRI could determine the entity (physiological vs. pathological) and origin (pancreatic vs. extrapancreatic) of upper abdominal increased DOTATOC uptake in significantly more patients compared with ^{68}Ga-DOTATOC PET/CT, resulting in considerable reduction in inconclusive PET images [82]. In the study performed by Afshar-Oromieh et al. in 2014, they tried to compare their results in prostate cancer detection after injection of ^{68}Ga-PSMA, and they concluded that PCa was detected more easily and more accurately with ^{68}Ga-PSMA PET/MRI than with PET/CT and with lower radiation exposure. Consequently, this new technique could clarify unclear findings on PET/CT [32]. With PET/MRI, different diagnostic sequences, higher contrast of lesions, and higher resolution of MRI enabled a subjectively easier evaluation of the images [32].

According to the studies, we decided to collect all important papers that have been published between 2008 and the end of 2015 and used dual-modality probes for PET/MRI and SPECT/MRI and evaluated their detection efficiency and targeting capability (their tumor and target uptakes). One of the most essential parameters for evaluating the efficiency of a contrast agent is their uptakes in tumor in comparison with other organs (especially crucial organs such as glands). By using dual-modality probe, we can assess the tumor uptake not only qualitatively but also quantitatively. This is much important when we have a PET/MRI probe for better uptake assessments. Due to the importance of PET/MRI and because the developments in dual-modality probes tend to PET/MRI at the end of this section, we draw your attention to the papers that are studied on the development of new and novel dual-modality contrast agents in SPECT/MRI and PET/MRI. Lahooti et al. extracted important data from the 50 different studies regarding dual-modality probes in PET/MRI or SPECT/MRI from 2008 to the end of 2015; they gathered all data and explain their results extensively in a systematic review paper, part of their data represented in Table 7.2 [44].

Table 7.2 Characterizations of multimodality contrast agents from selected studies

Compound	Size	Core	Coating	Targets	Uptakes	T_1 or T_2 contrast agent	Applications	Ref.
^{68}Ga-SPION	30 nm	Super paramagnetic iron oxide nanoparticles (SPIONs) ~13 nm	Polyethylene glycol (PEG)	Sentinel lymph nodes (SLN) and iliac lymph nodes	SLN, 123% IA/g Iliac lymph node, 47% IA/g Liver, 0.3% IA/g Spleen, 0.1% IA/g Kidneys, 0.05% IA/g 3 h postinjection (pi)	T_2- and T_2*-weighted imaging	PET/MRI for SLN mapping	[83]
^{68}Ga-SPION	85 nm	8.86 ± 1.61 nm iron oxide	PEG	Liver and spleen	At 1 hpi, Liver, 56.4% ID/g Spleen, 20.8% ID/g At 2 hpi Liver, 60.6% ID/g Spleen, 12.6% ID/g	T_2- and T_2*-weighted imaging	PET/MRI for the liver and spleen	[84]
^{68}Ga-NOTA-hydrazine-Fe_3O_4NPs (GaNHFCNP)	15.3 nm	Fe_3O_4NPs (11.5 nm)	Not reported	Colon cancer cell (CT-26) and breast cancer cell (SK-BR-3)	CT-26 cell line, 8.778% SK-BR-3 cell line, 15.491% 2 hpi	Not reported	Dual PET/MRI imaging of colon cancer cell (CT-26) and breast cancer cell (SK-BR-3)	[85]
^{68}Ga-NODAGA-AGuIX and ^{68}Ga-DOTAGA-AGuIX	2.5 ± 0.1 nm	Gadolinium oxide (Gd_2O_3) 1.7 nm	Polysiloxane	U87MG (human primary glioblastoma cell line)	Kidney, 22.4% ID/g Blood, 0.62% ID/g 2 hpi	T_1-weighted imaging $r_1 = 10.3\ mM^{-1}\ s^{-1}$ and $r_2 = 13.4\ mM^{-1}\ s^{-1}$ at 60 MHz	Dual PET/MRI contrast agent	[86]

Continued

Table 7.2 Characterizations of multimodality contrast agents from selected studies—cont'd

Compound	Size	Core	Coating	Targets	Uptakes	T_1 or T_2 contrast agent	Applications	Ref.
$^{68}Ga/^{111}In$-IONP	100 nm	10 nm Fe_2O_3	Aminosilane coating with NH_2	RES and efficient cell labeling	Liver, 2.18 ± 0.05, 2.74 ± 0.29, and 2.33 ± 0.2% ID/g Spleen, 1.46 ± 0.02, 4.24 ± 0.21, and 5.06 ± 0.25% ID/g Kidneys, 4.67 ± 0.08, 6.3 ± 0.35, and 7.91 ± 0.34% ID/g Blood, 4.67 ± 0.52, 1.82 ± 0.28, and 0.98 ± 0.24% ID/g Lung, 14.98 ± 1.22, 3.24 ± 0.85, and 1.16 ± 0.13% ID/g 2, 24 and 48 hpi	T_2-weighted imaging	Dual PET/MRI contrast agent	[87]
^{68}Ga-NOTA-OA-IONP	66 nm	Iron oxide 16 nm	PEG	Colon cancer (HT-29) cells	Tumor, 3.07 ± 0.76% ID/g 1 hpi	T_2-weighted imaging $r_2 = 157\ s^{-1}\ mM^{-1}$ at 200 MHz	Dual PET/MRI imaging agent for tumor diagnosis and analysis of tumor functionality and simultaneous tumor	[88]
^{68}Ga-NOTA-IO-Man	10.12 ± 1.46 nm	Iron oxide 5 nm	PEG	Lymph nodes	High LN uptakes after 30 min postfootpad injection	T_2-weighted imaging $r_2 = 449.9\ mM^{-1}\ s^{-1}$ at 600 MHz	Dual PET/MRI contrast agent	[89]

^{68}Ga-NODA-Magh-1-PNPs	44 ± 55 nm	Iron oxide (Fe_2O_3) 8–12 nm	PLGA-b-PEG-COOH	A promising tool for innovative PET/MRI diagnostic agents	Liver, 2.2% ID/g Spleen, 2% ID/g Kidney, 0.5% ID/g Lung, 0.6% ID/g Heart, 0.3% ID/g (20,60,120, and 180 min post injection)	$r_2 = 182\ mM^{-1}\ s^{-1}$ $r_1 = 0.5\ mM^{-1}\ s^{-1}$at 60 MHz	PET/MRI for targeted imaging	[90]
^{68}Ga-DOTA-IO-GUL (glutamate-urea-lysine)	11.01 ± 1.54 nm	5 nm iron oxide	PEG	Prostate-specific membrane antigen (PSMA)	Tumor uptakes, 5.34% ID after 1 h post-i.v. injection SUV for tumor was 2.385 from PET images	T_2-weighted $r_2 = 185.13\ mM^{-1}\ s^{-1}$	PET/MRI for targeted imaging	[91]
^{64}Cu-NOTA-SPION-cRGD-DOX	68 ± 2 nm	SPION 10 nm	Hetero bifunctional poly (ethylene glycol) (PEG)	U87MG cells (human glioblastoma cells)	Tumor, 5.6 ± 1.7% ID/g Liver, 9.7 ± 2.7% ID/g Blood, 1.8 ± 0.3% ID/g 6 hpi	T_2-weighted imaging $101.9\ mM^{-1}\ s^{-1}$ at 200 MHz	Combined tumor targeting drug delivery and PET/MR imaging	[92]
^{64}Cu-DOTA-IO-RGD	45 ± 10 nm	Iron oxide 5 nm	Polyaspartic acid (PASP)	U87MG human glioblastoma cell line, tumor $\alpha_v\beta_3$ integrin expression	Liver, 22.6 ± 2.9% ID/g Kidney, 4.9 ± 0.8% ID/g Tumor, 10.1 ± 2.1% ID/g 4 hpi	T_2-weighted imaging $105.5\ mM^{-1}\ s^{-1}$	Dual PET/MRI scanning of tumor integrin $\alpha_v\beta_3$ expression	[93]
$^{64}Cu^{II}$-dtcbp-SPION	108 ± 60 nm	SPION	Dextran	Draining lymph nodes	The popliteal lymph nodes and the iliac lymph nodes	T_2*-weighted imaging	PET/MRI for lymph node mapping	[94]
^{64}Cu-DOTA-mSPIO	20.3 ± 1.9 nm	SPION 6.2 nm	PEG + micelle	Heart and carotid arteries (atherosclerosis and cancer models)	Liver, 33.42 ± 1.85% ID/g Spleen, 19.96 ± 2.27% ID/g Heart, 9.46 ± 1.76% ID/g Blood, 37.31 ± 12.87% ID/g 1 hpi	T_2-weighted imaging $209 \pm 26\ mM^{-1}\ s^{-1}$ at 20 MHz	PET/MRI for disease detection and treatment in atherosclerosis and cancer models	[95]

Continued

Table 7.2 Characterizations of multimodality contrast agents from selected studies—cont'd

Compound	Size	Core	Coating	Targets	Uptakes	T_1 or T_2 contrast agent	Applications	Ref.
^{64}Cu-MoS_2-IO-(d) PEG	Not reported	MoS_2 50–200 nm	PEG	Breast cancer (4T1 tumor)	Tumor, 5.70% ID/g Liver, 30% ID/g Spleen, 11% ID/g 24 hpi	T_2-weighted imaging 93.59 mM^{-1} s^{-1} at 128 MHz	Triple modal PET, PAT, and MR imaging for 4T1 murine breast tumor	[96]
^{64}Cu-DOTA-MSN-Gd^{+3}	76.8 ± 8.3 nm	Mesoporous silica nanoparticles (60 nm)	Not reported	Sentinel lymph nodes (SLNs)	T-SLNs, 76.7 ± 2.21% ID/g N-SLNs, 2.3 ± 0.12% ID/g 1 hpi	T_1-weighted imaging	Mapping SLNs and identifying tumor metastasis	[85]
^{64}Cu-TNP or ^{64}Cu-DTPA (^{64}Cu-DTPA-CLIO-VT680)	20 nm	5 nm iron oxide	Dextran	Inflammatory atherosclerotic plaques	Blood half-life, $T_{1/2}$ 259 ± 39 min Liver, 33.6% ID/g Small Intestine, 15.8% ID/g Kidney, 13.8% ID/g Lung, 11.0% ID/g Spleen, 9.4% ID/g Heart, 6.0% ID/g Aorta, 5.2% ID/g Lymph nodes, 4.3% ID/g Thymus, 2.4% ID/g 24 hpi	T_2-weighted imaging	Triple PET/MRI/optical contrast agent	[97]
^{64}Cu-bisphosphonate-$MnFe_2O_4$ and [18 F]-fluoride-$MnFe_2O_4$	49.8 nm	$MnFe_2O_4$ 4.8 nm	$Al(OH)_3$ PEG (5 K)	The ability to derivatize the surface with radiolabels and bisphosphonate groups suggests applications in molecular imaging	Liver and spleen	T_2- and T_2*-weighted imaging $r_2 = 121.9$ mM^{-1} s^{-1}at 128 MHz	Dual PET/MRI contrast agent	[98]
^{64}Cu-Cy5.5-IONPs	19 nm	15 nm iron oxide	Dopamine and albumin (HSA)	Not reported	Tumor, 5.46, 6.11, and 8.45% ID/gat 1, 4, and 18 hpi	T_2-weighted imaging $r_2 = 314.5$ mM^{-1} s^{-1} at 300 MHz	PET/MR/Optical nude micebearing U87MG tumors	[99]

^{64}Cu-DOTA-IO-c (RGDyK)	12 nm	8 nm iron oxide	Ferritin	For tumor visualization of nude mice bearing U87MG tumors	Tumor, 6.4, 7.5, 8.1, and 7.5% ID/g at 1, 4, 24, and 40 hpi	T_2- and T_2*-weighted imaging	Triple PET/MR/NIRF	[100]
^{64}Cu-DOTA-GdVO4:4%Eu-DGEA	Thickness = 5 nm and width = 150 nm	Gd	OA PAA	Prostate cancer, high $\alpha_v\beta_3$ integrin expression	Tumor/background contrast, 8.4% ID/g 20–24 hpi Tumor 7.2% ID/g 45 hpi	T_1-weighted imaging	Dual PET/MRI contrast agent of integrin $\alpha_v\beta_3$ expression in prostate cancer	[101]
^{64}Cu-DOTA-USPIOn	140 ± 7 nm	USPION 5 nm	PEG	MDA-MB-231 Human breast cancer cell	Tumor, 3.5 ± 0.25% ID/g Liver, 22.0 ± 6.0% ID/g 20 hpi	T_2-weighted imaging $r_2 = 265 \pm 10\ s^{-1}\ mM^{-1}$ $r_2/r_1 = 123$ at 60 MHz	Dual PET/MRI contrast agent	[102]
^{18}F/^{64}Cu-$Co_{0.16}Fe_{2.84}O_4$@$NaYF_4$(Yb, Er)-BP-PEG	44 nm	Fe_3O_4@$NaYF_4$ and $Co_{0.16}Fe_{2.84}O_4$ @$NaYF_4$(Yb, Er) 10.3 ± 1.4 nm	PEG 2 K and PEG 10 K	NPs cleared from the blood pool more slowly than positively charged NPs	With 10 K PEG and lower charge −10 mV, Liver, 24.3, 32.1, 43.1, and 34.3% ID Blood, 22.7, 17.2, 8.6, and 6.5% ID Spleen, 2% ID Bone, 16.3, 17.2, 17.5, and 23.4% ID With 2 K PEG and lower charge +10 mV, Liver, 49.6, 66.4, 53.8, and 44.9% ID Blood, 7.3, 1.6, 1.4, and 0.9% ID Bone, 11.1, 10.1, 15.2, and 21.1% ID Spleen, 3.3, 3.4, 3.1, and 3.0% ID at 15, 45, 75, and 120 min pi, respectively	T_2-weighted imaging $r_2 = 325.9 \pm 10$ and $r_1 = 2.7 \pm 0.1\ mM^{-1}\ s^{-1}$ for PEG 2 K $r_2 = 102 \pm 2.6$ and $r_1 = 5 \pm 0.6\ mM^{-1}\ s^{-1}$ for PEG 10 K at 128 MHz	Dual PET/MRI contrast agent	[103]

Continued

Table 7.2 Characterizations of multimodality contrast agents from selected studies—cont'd

Compound	Size	Core	Coating	Targets	Uptakes	T_1 or T_2 contrast agent	Applications	Ref.
^{64}Cu-Apoferretin	13.6 nm	Fe_2O_3 12.1 nm	Apoferretin	Good tumor uptake for human colon cancer	Tumor, 4.82, 6.14, 7.34, 7.26, and 6.74% ID/g at 1, 2, 4, 18, and 26 hpi	T_1-weighted $r_1 = 2.54\ mM^{-1}\ s^{-1}$ at 60 MHz	PET/MRI/photo acoustic imaging	[104]
^{64}Cu-RGD-PEG-MNP	9.6 nm	4.5 ± 0.5 nm USPIO	PEG	Glioma tumor and $\alpha_v\beta_3$ integrin U87MG cells	Tumor, 4.13, 5.79, and 5.95% ID/g Liver, 22.76, 22.43, and 15.86% ID/g Spleen, 7.11, 6.94, and 6.62% ID/g at 2, 4, 24 hpi	$r_1 = 1.2\ mM^{-1}\ s^{-1}$ at 400 MHz	PET/MRI for tumor targeting	[105]
^{64}Cu-DOTA-IO	26.6 ± 7.3 nm	Iron oxide 7.9 ± 2.0 nm	Dextran	Macrophages	Atherosclerosis plaques	T_2- and T_2*-weighted imaging $r_1 = 14.46$ and $r_2 = 72.6\ s^{-1}\ mM^{-1}$ at 60 MHz	Dual PET/MRI probe for cardiovascular imaging of plaques	[106, 107]
^{18}F-CLIO	38 nm	3 nm iron oxide	Cross-linked dextran	Aortic aneurysms (AAs)	Blood half-life, $T_{1/2} = 192 \pm 14$ min	T_2-weighted imaging	PET/MRI quantitation of macrophage content in a mouse model of AAs	[108]
^{11}C-SPION	NM	SPION 16 nm	COOH	Liver	Liver	T_2*-weighted imaging	PET/MRI of the liver	[109]
^{124}I-SA-MnMEIO	32 nm	MnMEIO 15 nm	Serum albumin (SA)	Sentinel lymph node	High lymph node uptake at 1 h postinjection to the forepaw and they still remain until 6 days post injection	T_2-weighted imaging $321.6\ mM^{-1}\ s^{-1}$	Axillary and brachial lymph nodes imaging PET/MRI	[110]
^{124}I-c(RGDyk)$_2$-UCNPs	32 ± 9 nm	Upconversion nanophosphors ($NaGdF_4/Er^{3+}/Yb^{3+}$)	PEG	$\alpha_v\beta_3$ integrin expression tumors, U87MG tumor cells, and xeno grafted tumor	Tumor, 2.8 ± 0.8% ID/g	T_1-weighted imaging	Dual PET/MRI scanning of tumor integrin $\alpha_v\beta_3$ expression	[111]

^{124}I-TCL-SPION	40 nm	4–11 nm iron oxide	Cross-linked PEG	Not reported	No quantification but images show uptakes in tumor and lymph nodes (front paw injection)	T_2-weighted imaging $r_2 = 283.7\ mM^{-1}\ s^{-1}$ at 60 MHz	Triple-modality optical/PET/MR imaging imaging of 4T1 breast tumor	[112]
^{69}Ge-SPION (chelator-free strategy)	23 nm	SPION 10 nm	PEG	Sentinel lymph node	Dominant liver uptake, spleen, popliteal lymph node	T_2*-weighted imaging	Lymph node mapping PET/MRI	[113]
^{99m}Tc-DPA-ale-Endorem	106 ± 6 nm	SPION 5 nm	Dextran	RES system (liver and spleen)	Liver, 96.9 ± 0.9% ID Spleen, 1.3 ± 0.4% ID Rest of body, 1.8 ± 0.7% ID 1 hpi	T_2*-weighted imaging 26 $mM^{-1}\ s^{-1}$ at 400 MHz	Dual-modality probe for SPECT/MRI for RES system imaging	[114]
^{99m}Tc-DTPA-SPION-LBA	30 nm	SPION 12 nm	Dopamine	ASGP-R on hepatocytes	Liver, 38.43 ± 6.45% ID/g Spleen, 18.69 ± 5.12% ID/g Blood, 4.88 ± 1.18% ID/g 1 hpi	T_2-weighted imaging	SPECT/MRI for hepatocyte targeted imaging and the diagnosis of various liver diseases	[115]
^{99m}Tc-SPION-RGD	200 nm	SPION 10 ± 2 nm	Aminosilane	$\alpha_v\beta_3$ integrin receptors in U87MG glioblastoma cells	Tumor, 9.01 ± 0.19% ID/g Liver, 10.36 ± 0.87% ID/g Spleen, 31.14 ± 3.78% ID/g Blood, 8.88 ± 0.19% ID/g 1 hpi	T_2-weighted imaging	Dual SPECT/MRI scanning of tumor integrin $\alpha_v\beta_3$ expression	[116]
^{99m}Tc-SPIONs	18 nm	13 nm iron oxide	PEG	Sentinel lymph node	SLN, 211 ± 225% ID/g Liver, 1.4 ± 0.7% ID/g Kidney, 0.3 ± 0.08% ID/g Spleen, 0.2 ± 0.1% ID/g 4 hpi	T_2- and T_2*-weighted imaging	Dual SPECT/MRI for Sentinel lymph node (SLN) mapping in breast cancer and malignant melanoma	[117]
^{99m}Tc-USPIO	80 nm	5 nm iron oxide	Cross-linked dextran	Liver and spleen (RES)	Liver and spleen, 78% ID/g 15 min pi 25% ID/g 48 hpi	T_2- and T_2*-weighted imaging	Dual SPECT/MRI for RES theranostic purposes	[118]

Continued

Table 7.2 Characterizations of multimodality contrast agents from selected studies—cont'd

Compound	Size	Core	Coating	Targets	Uptakes	T_1 or T_2 contrast agent	Applications	Ref.
^{99m}Tc-USPIO	41 nm	5 nm iron oxide	Cross-linked dextran	Liver and spleen (RES)	Liver, 55.11% ID/g Spleen, 19.75% ID/g 5 min pi Liver, 30.91% ID/g Spleen, 10.68% ID/g 1 hpi Blood half-life was 90 s	T_2- and T_2*-weighted imaging	Dual SPECT/MRI for RES theranostic purposes	[119]
^{99m}Tc-USPIO-C595	114 nm	5 nm iron oxide	Cross-linked dextran	Breast cancer and RES	Very promising *in vitro* results but low *in vivo* tumor uptakes due to the protein corona effect	T_2- and T_2*-weighted imaging	Dual SPECT/MRI for breast cancer	[120]
^{111}In-DMPE-DTPA-SPION	40 ± 7 nm	SPION	PEG	Not reported	Liver, 37.28 ± 1.03% ID/g Spleen, 21.48 ± 2.41% ID/g 24 hpi	Not reported	Not reported	[121]
^{111}In-DOTA-di-scFv-c	20 nm	Iron oxide 5 nm	Dextran PEG	Glandular epithelial cells express MUC-1	Tumor, 6% ID/g Liver, 23% ID/g Spleen, 9% ID/g Kidney, 7% ID/g 48 hpi	T_2-weighted imaging	Dual SPECT/MRI of MUC-1 expression in glandular epithelial cells	[122]
^{111}In-mAbMB-SPION	69.6 nm	17 nm iron oxide	Carboxymethyl dextran	^{111}In-labeled antimesothelin antibody with SPIONs	Liver, 2.1, 8.1% ID/g Spleen, 28.6, 48.4% ID/g Tumor, 2.2, 3.8% ID/g at 24 hpi and 72 hpi	T_2- and T_2*-weighted imaging	For SPECT/MR imaging of mesothelioma	[123]
^{111}In-IONPS-ChL6	20, 30, and 100 nm	5 nm iron oxide	PEG-dextran	Breast cancer	Tumor % ID/g ± SD of each SPIO 20 nm, 9.00 ± 0.8% ID/g 30 nm, 3.0 ± 0.3% ID/g 100 nm, 4.5 ± 0.8% ID/g 48 hpi	T_2- and T_2*-weighted imaging	Dual SPECT/MRI for breast alternating magnetic field (AMF) therapy	[124]

^{125}I-cRGD-USPIO	51.3 nm	Iron Oxide	Carboxymethyl dextran (CMD)	$\alpha_v\beta_3$ integrin receptors	Kidney, 11.60% ID/g Liver, 9.28 ± 1.04% ID/g Blood, 47.60 ± 6.63 and 2% ID/g in 1 and 48 hpi Liver, 9.28 ± 1.04,6.65 ± 0.33 and 1.69 ± 0.08% ID/g at 1, 4, and 24 hpi Spleen, 8.08 ± 1.09, 4.96 ± 0.16 and 1.34 ± 0.06% ID/g at 1, 4, and 24 hpi Tumor, 3.73 ± 2.40, 8.08 ± 0.30 and 3.65% ID/g at 1, 4, and 24 hpi	T_2-weighted imaging	Dual SPECT/MRI of integrin $\alpha_v\beta_3$ expression in breast cancer	[125]
^{125}I-Fe_3O_4-Ag heterodimers	Not reported	Fe_3O_4-Ag 14 nm	PEG	Not reported	Liver, 31.98 ± 2.44% ID/g Spleen, 41.87 ± 4.41% ID/g 1 hpi	T_2-weighted imaging 139.8 mM^{-1} s^{-1} at 60 MHz	Dual-modality probe in SPECT/MRI	[126]
^{59}Fe-SPION	17 ± 6 nm	SPION 4.3 ± 1.3 nm	PAA-DOP-PEG	Not reported	Liver, 45 ± 6% ID/g Kidneys, 21 ± 5% ID/g Brain, 4 ± 6% ID/g 24 hpi	T_1- and $^*T_2$-weighted imaging 97 ± 3 mM^{-1} s^{-1} at 300 MHz	Dual-modality probe in SPECT/MRI	[127]
^{89}Zr-DFO-ferumoxytol	Not reported	Iron oxide 15–35 nm	Carboxymethyl dextran	Prostate cancer and lymph node	Liver, kidney, axillary, and brachial lymph nodes	T_2- or T_2^*-weighted imaging 89 mM^{-1} s^{-1} at 20 MHz	SPECT/MRI for diverse nanomedical diagnostic applications	[128]
^{67}Ga-NOTA-MF-AS1411	68.1 nm	Cobalt ferrite	Silica and PEG	Nucleolin (a cellular membrane protein highly expressed in cancer) C6 rat glioma cells	Intestine, liver, and tumors	T_2-weighted imaging 82.1 mM^{-1} s^{-1} at 60 MHz	Targeting nucleolin and monitoring by multimodal fluorescent, radioisotope, and SPECT/MRI modalities	[129]

Continued

Table 7.2 Characterizations of multimodality contrast agents from selected studies—cont'd

Compound	Size	Core	Coating	Targets	Uptakes	T_1 or T_2 contrast agent	Applications	Ref.
^{67}Ga-DTPA-USPIO	85 nm	5 nm iron oxide	Cross-linked dextran	Liver and spleen (RES)	Liver, 62.25 and 22.75% ID/g Spleen, 23.03 and 5.27% ID/g at 15 min pi and 2 days pi	T_2- and T_2*-weighted imaging $r_2 = 16.3\ mM^{-1}\ s^{-1}$ and $r_1 = 0.41\ mM^{-1}\ s^{-1}$ at 60 MHz	Dual SPECT/MRI for RES theranostic purposes	[130]
^{166}Ho-DTPA-SPION	85 nm	7 nm iron oxide	Dextran	Liver and spleen (RES)	Liver, 60.1% ID/g Spleen, 15.3% ID/g 30 min pi	T_2- and T_2*-weighted imaging	Dual SPECT/MRI for RES theranostic purposes	[131]

REFERENCES

[1] B.J. Pichler, M.S. Judenhofer, C. Pfannenberg, Multimodal imaging approaches: PET/CT and PET/MRI, Handb. Exp. Pharmacol. 185 (2008) 109–132.
[2] D.W. Townsend, Dual-modality imaging: combining anatomy and function, J. Nucl. Med. 49 (2008) 938–955.
[3] M.D. Seemann, Whole-body PET/MRI: the future in oncological imaging, Technol. Cancer Res. Treat. 4 (2005) 577–582.
[4] B.E. Hammer, NMR-PET scanner apparatus, Google Patents, 1990.
[5] B.E. Hammer, N.L. Christensen, B.G. Heil, Use of a magnetic field to increase the spatial resolution of positron emission tomography, Med. Phys. 21 (1994) 1917–1920.
[6] J. Wischhusen, J.-G. Delcros, P. Mehlen, F. Padilla, Detection of tumoral netrin-1 protein levels using ultrasound microbubble contrast agents: in vitro validation, J. Acoust. Soc. Am. 140 (2016) 3369.
[7] S. Rathnayake, J. Mongan, A.S. Torres, R. Colborn, D.W. Gao, B.M. Yeh, Y. Fu, In vivo comparison of tantalum, tungsten, and bismuth enteric contrast agents to complement intravenous iodine for double-contrast dual-energy CT of the bowel, Contrast Media Mol. Imaging 11 (4) (2016) 254–261.
[8] J. Qin, C. Peng, B. Zhao, K. Ye, F. Yuan, Z. Peng, X. Yang, L. Huang, M. Jiang, Q. Zhao, G. Tang, X. Lu, Noninvasive detection of macrophages in atherosclerotic lesions by computed tomography enhanced with PEGylated gold nanoparticles, Int. J. Nanomed. 9 (2014) 5575–5590.
[9] A. Lahooti, S. Shanehsazzadeh, A.R. Jalilian, M.B. Tavakoli, Assessment of effective absorbed dose of 111In-DTPA-Buserelin in human on the basis of biodistribution rat data, Radiat. Prot. Dosim. 154 (2013) 1–8.
[10] S. Shanehsazzadeh, A. Lahooti, S.P. Shirmardi, M. Erfani, Comparison of estimated human effective dose of 67Ga-and 99mTc-labeled bombesin based on distribution data in mice, J. Radioanal. Nucl. Chem. 305 (2015) 513–520.
[11] S. Shanehsazzadeh, H. Yousefnia, A. Lahooti, S. Zolghadri, A.R. Jalilian, H. Afarideh, Assessment of human effective absorbed dose of 67 Ga–ECC based on biodistribution rat data, Ann. Nucl. Med. 29 (2015) 118–124.
[12] A.R. Jalilian, S. Shanesazzadeh, P. Rowshanfarzad, F. Bolourinovin, A. Majdabadi, Biodistribution study of [61 Cu] pyruvaldehyde-bis (N-4-methylthiosemicarbazone) in normal rats as a PET tracer, Nucl. Sci. Tech. 19 (2008) 159–164.
[13] S. Shanehsazzadeh, A. Lahooti, H. Yousefnia, P. Geramifar, A.R. Jalilian, Comparison of estimated human dose of 68Ga-MAA with 99mTc-MAA based on rat data, Ann. Nucl. Med. 29 (2015) 745–753.
[14] J. Specht, S. Partridge, X. Chai, A. Novakova, L. Peterson, A. Shields, J. Guenthoer, H. Linden, J. Gralow, V. Gadi, Abstract P5-01-02: multimodality molecular imaging with dynamic 18 F-fluorodeoxyglucose positron emission tomography (FDG PET) and MRI to evaluate response and resistance to neoadjuvant chemotherapy (NAC), Cancer Res. 76 (2016). P5-01-02-P05-01-02.
[15] C. Johnbeck, U. Knigge, A. Loft, A. Berthelsen, J. Mortensen, P. Oturai, S. Langer, D. Elema, A. Kjaer, Head to Head comparison of 64Cu-DOTATATE and 68Ga-DOTATOC PET/CT: a prospective study of 59 patients with neuroendocrine tumors, J. Nucl. Med. 57 (2016) 151.
[16] Y. Fazaeli, S. Shanehsazzadeh, A. Lahooti, S. Feizi, A. Jalilian, Preclinical dosimetric estimation of [111In] 5, 10, 15, 20-tetra phenyl porphyrin complex as a possible imaging/PDT agent, Radiochim. Acta 104 (2016) 327–336.
[17] J.D. Freedman, H. Lusic, M. Wiewiorski, M. Farley, B.D. Snyder, M.W. Grinstaff, A cationic gadolinium contrast agent for magnetic resonance imaging of cartilage, Chem. Commun. 51 (2015) 11166–11169.

[18] K. An, H.B. Na, Y.I. Park, S.H. Choi, J.S. Son, N. Lee, Hollow MnOxPy and Pt/MnOxPy yolk/shell nanoparticles as a T1 MRI contrast agent, J. Colloid Interface Sci. 439 (2015) 134–138.
[19] D. Patel, A. Kell, B. Simard, B. Xiang, H.Y. Lin, G. Tian, The cell labeling efficacy, cytotoxicity and relaxivity of copper-activated MRI/PET imaging contrast agents, Biomaterials 32 (2011) 1167–1176.
[20] P. Bouziotis, D. Psimadas, T. Tsotakos, D. Stamopoulos, C. Tsoukalas, Radiolabeled iron oxide nanoparticles as dual-modality SPECT/MRI and PET/MRI agents, Curr. Top. Med. Chem. 12 (2012) 2694–2702.
[21] H.-P.W. Schlemmer, B.J. Pichler, M. Schmand, Z. Burbar, C. Michel, R. Ladebeck, K. Jattke, D. Townsend, C. Nahmias, P.K. Jacob, Simultaneous MR/PET imaging of the human brain: feasibility study, Radiology 248 (2008) 1028–1035.
[22] H. Kurihara, C. Shimizu, Y. Miyakita, M. Yoshida, A. Hamada, Y. Kanayama, K. Yonemori, J. Hashimoto, H. Tani, M. Kodaira, Molecular imaging using PET for breast cancer, Breast Cancer 23 (1) (2016) 24–32.
[23] M.L. James, S.S. Gambhir, A molecular imaging primer: modalities, imaging agents, and applications, Physiol. Rev. 92 (2012) 897–965.
[24] H. Boll, S. Nittka, F. Doyon, M. Neumaier, A. Marx, M. Kramer, C. Groden, M. A. Brockmann, Micro-CT based experimental liver imaging using a nanoparticulate contrast agent: a longitudinal study in mice, PLoS One 6 (2011) e25692.
[25] A.-C. Roessler, M. Hupfer, D. Kolditz, G. Jost, H. Pietsch, W.A. Kalender, High atomic number contrast media offer potential for radiation dose reduction in contrast-enhanced computed tomography, Invest. Radiol. 51 (2016) 249–254.
[26] R. Gessner, P.A. Dayton, Advances in molecular imaging with ultrasound, Mol. Imaging 9 (2010) 117–127.
[27] H.-D. Liang, M.J.K. Blomley, The role of ultrasound in molecular imaging, Br. J. Radiol. 76 (2003) S140–S150.
[28] M.L. Schroeter, Optische Bildgebung in der kognitiven Neurowissenschaft, Universität Leipzig, Leipzig, 2006.
[29] R. Thomas, I.-K. Park, Y.Y. Jeong, Magnetic iron oxide nanoparticles for multimodal imaging and therapy of cancer, Int. J. Mol. Sci. 14 (2013) 15910–15930.
[30] S. Sharifi, H. Seyednejad, S. Laurent, F. Atyabi, A.A. Saei, M. Mahmoudi, Superparamagnetic iron oxide nanoparticles for in vivo molecular and cellular imaging, Contrast Media Mol. Imaging 10 (5) (2015) 329–355.
[31] A. Boss, S. Bisdas, A. Kolb, M. Hofmann, U. Ernemann, C.D. Claussen, C. Pfannenberg, B.J. Pichler, M. Reimold, L. Stegger, Hybrid PET/MRI of intracranial masses: initial experiences and comparison to PET/CT, J. Nucl. Med. 51 (2010) 1198–1205.
[32] A. Afshar-Oromieh, U. Haberkorn, H.P. Schlemmer, M. Fenchel, M. Eder, M. Eisenhut, B.A. Hadaschik, A. Kopp-Schneider, M. Röthke, Comparison of PET/CT and PET/MRI hybrid systems using a 68Ga-labelled PSMA ligand for the diagnosis of recurrent prostate cancer: initial experience, Eur. J. Nucl. Med. Mol. Imaging 41 (2014) 887–897.
[33] E. Gellén, O. Sántha, E. Janka, I. Juhász, Z. Péter, I. Erdei, R. Lukács, N. Fedinecz, L. Galuska, É. Remenyik, G. Emri, Diagnostic accuracy of 18 F-FDG-PET/CT in early and late stages of high-risk cutaneous malignant melanoma, J. Eur. Acad. Dermatol. Venereol. 29 (10) (2015) 1938–1944.
[34] P. Veit-Haibach, F. Kuhn, F. Wiesinger, G. Delso, G. von Schulthess, PET–MR imaging using a tri-modality PET/CT–MR system with a dedicated shuttle in clinical routine, Magn. Reson. Mater. Phys. 26 (2013) 25–35.
[35] Y. Assiri, P. Veit-Haibach, Contrast-enhanced PET/CT vs. non-contrast enhanced PET/MRI in abdominal oncological lesions-initial results, Eur. J. Nucl. Med. Mol. Imaging (2012) S189–S190. Springer, 233 Spring St, New York, NY 10013, USA.

[36] N.F. Schwenzer, C. Schraml, M. Müller, C. Brendle, A. Sauter, W. Spengler, A.C. Pfannenberg, C.D. Claussen, H. Schmidt, Pulmonary lesion assessment: comparison of whole-body hybrid MR/PET and PET/CT imaging—pilot study, Radiology 264 (2012) 551–558.
[37] V. Stefaan, K.M. Paul, PET-MRI: a review of challenges and solutions in the development of integrated multimodality imaging, Phys. Med. Biol. 60 (2015) R115–R154.
[38] P. Appenzeller, C. Mader, D. Schmidt, D. Schmid, P. Veit-Haibach, Low-dose PET/CT vs. fast body coil PET/MRI-how low can you go? Eur. J. Nucl. Med. Mol. Imaging (2012) S175. Springer, 233 Spring St, New York, NY 10013, USA.
[39] A.W. Sauter, H.F. Wehrl, A. Kolb, M.S. Judenhofer, B.J. Pichler, Combined PET/MRI: one step further in multimodality imaging, Trends Mol. Med. 16 (2010) 508–515.
[40] B.J. Pichler, A. Kolb, T. Nägele, H.-P. Schlemmer, PET/MRI: paving the way for the next generation of clinical multimodality imaging applications, J. Nucl. Med. 51 (2010) 333–336.
[41] T.J. Fraum, K.J. Fowler, J. McConathy, E.E. Parent, F. Dehdashti, P.W. Grigsby, B.A. Siegel, PET/MRI for the body imager: abdominal and pelvic oncologic applications, Abdom. Imaging 40 (2015) 1387–1404.
[42] B.R. Jarrett, B. Gustafsson, D.L. Kukis, A.Y. Louie, Synthesis of 64Cu-labeled magnetic nanoparticles for multimodal imaging, Bioconjug. Chem. 19 (2008) 1496–1504.
[43] C. Nappi, M. Altiero, M. Imbriaco, E. Nicolai, C.A. Giudice, M. Aiello, C. T. Diomiaiuti, A. Pisani, L. Spinelli, A. Cuocolo, First experience of simultaneous PET/MRI for the early detection of cardiac involvement in patients with Anderson-Fabry disease, Eur. J. Nucl. Med. Mol. Imaging 42 (2015) 1025–1031.
[44] A. Lahooti, S. Sarkar, S. Laurent, S. Shanehsazzadeh, Dual nano-sized contrast agents in PET/MRI: a systematic review, Contrast Media Mol. Imaging 11 (2016) 428–447.
[45] G.K. von Schulthess, H.-P.W. Schlemmer, A look ahead: PET/MR versus PET/CT, Eur. J. Nucl. Med. Mol. Imaging 36 (2009) 3–9.
[46] P. Marzola, F. Osculati, A. Sbarbati, High field MRI in preclinical research, Eur. J. Radiol. 48 (2003) 165–170.
[47] G. Antoch, A. Bockisch, Combined PET/MRI: a new dimension in whole-body oncology imaging? Eur. J. Nucl. Med. Mol. Imaging 36 (2009) 113–120.
[48] V. Schulz, I. Torres-Espallardo, S. Renisch, Z. Hu, N. Ojha, P. Börnert, M. Perkuhn, T. Niendorf, W. Schäfer, H. Brockmann, Automatic, three-segment, MR-based attenuation correction for whole-body PET/MR data, Eur. J. Nucl. Med. Mol. Imaging 38 (2011) 138–152.
[49] M.K. Werner, H. Schmidt, N.F. Schwenzer, MR/PET: a new challenge in hybrid imaging, Am. J. Roentgenol. 199 (2012) 272–277.
[50] H.-P. Schlemmer, B.J. Pichler, R. Krieg, W.-D. Heiss, An integrated MR/PET system: prospective applications, Abdom. Imaging 34 (2009) 668–674.
[51] M.J. Paldino, D.P. Barboriak, Fundamentals of quantitative dynamic contrast-enhanced MR imaging, Magn. Reson. Imaging Clin. N. Am. 17 (2009) 277–289.
[52] H.C. Thoeny, B.D. Ross, Predicting and monitoring cancer treatment response with diffusion-weighted MRI, Magn. Reson. Med. 32 (2010) 2–16.
[53] D.-M. Koh, D.J. Collins, Diffusion-weighted MRI in the body: applications and challenges in oncology, Am. J. Roentgenol. 188 (2007) 1622–1635.
[54] C. Buchbender, T.A. Heusner, T.C. Lauenstein, A. Bockisch, G. Antoch, Oncologic PET/MRI, part 1: tumors of the brain, head and neck, chest, abdomen, and pelvis, J. Nucl. Med. 53 (2012) 928–938.
[55] M.G. Harisinghani, J. Barentsz, P.F. Hahn, W.M. Deserno, S. Tabatabaei, C.H. van de Kaa, J. de la Rosette, R. Weissleder, Noninvasive detection of clinically occult lymph-node metastases in prostate cancer, N. Engl. J. Med. 348 (2003) 2491–2499.

[56] S.G. Nekolla, A. Martinez-Moeller, A. Saraste, PET and MRI in cardiac imaging: from validation studies to integrated applications, Eur. J. Nucl. Med. Mol. Imaging 36 (2009) 121–130.
[57] K. Herholz, PET studies in dementia, Ann. Nucl. Med. 17 (2003) 79–89.
[58] M.J. Koepp, F.G. Woermann, Imaging structure and function in refractory focal epilepsy, Lancet Neurol. 4 (2005) 42–53.
[59] S.R. Teixeira, C. Martinez-Rios, L. Hu, B.A. Bangert, Clinical applications of pediatric positron emission tomography-magnetic resonance imaging, Semin. Roentgenol. 49 (4) (2014) 353–366.
[60] S. Vandenberghe, P.K. Marsden, PET-MRI: a review of challenges and solutions in the development of integrated multimodality imaging, Phys. Med. Biol. 60 (2015) R115–R154.
[61] H. Zaidi, N. Ojha, M. Morich, J. Griesmer, Z. Hu, P. Maniawski, O. Ratib, D. Izquierdo-Garcia, Z.A. Fayad, L. Shao, Design and performance evaluation of a whole-body Ingenuity TF PET-MRI system, Phys. Med. Biol. 56 (2011) 3091–3106.
[62] G. Delso, S. Furst, B. Jakoby, R. Ladebeck, C. Ganter, S.G. Nekolla, M. Schwaiger, S.I. Ziegler, Performance measurements of the Siemens mMR integrated whole-body PET/MR scanner, J. Nucl. Med. 52 (2011) 1914–1922.
[63] S.R. Cherry, Multimodality imaging: beyond PET/CT and SPECT/CT, Semin. Nucl. Med. 39 (5) (2009) 348–353.
[64] G. Delso, S. Ziegler, PET/MRI system design, Eur. J. Nucl. Med. Mol. Imaging 36 (2009) 86–92.
[65] A. Kalemis, B.M. Delattre, S. Heinzer, Sequential whole-body PET/MR scanner: concept, clinical use, and optimisation after two years in the clinic. The manufacturer's perspective, Magma (New York, N.Y.) 26 (2013) 5–23.
[66] B.J. Pichler, M.S. Judenhofer, C. Catana, J.H. Walton, M. Kneilling, R.E. Nutt, S. B. Siegel, C.D. Claussen, S.R. Cherry, Performance test of an LSO-APD detector in a 7-T MRI scanner for simultaneous PET/MRI, J. Nucl. Med. 47 (2006) 639–647.
[67] H. Zaidi, M.-L. Montandon, D.O. Slosman, Magnetic resonance imaging-guided attenuation and scatter corrections in three-dimensional brain positron emission tomography, Med. Phys. 30 (2003) 937–948.
[68] A. Salomon, A. Goedicke, B. Schweizer, T. Aach, V. Schulz, Simultaneous reconstruction of activity and attenuation for PET/MR, IEEE Trans. Med. Imaging 30 (2011) 804–813.
[69] D. Renker, New trends on photodetectors, Nucl. Instrum. Methods Phys. Res., Sect. A 571 (2007) 1–6.
[70] T.E. Yankeelov, T.E. Peterson, R.G. Abramson, D. Garcia-Izquierdo, L. R. Arlinghaus, X. Li, N.C. Atuegwu, C. Catana, H.C. Manning, Z.A. Fayad, Simultaneous PET-MRI in oncology: a solution looking for a problem? Magn. Reson. Med. 30 (2012) 1342–1356.
[71] C. Catana, A.R. Guimaraes, B.R. Rosen, PET and MR imaging: the odd couple or a match made in heaven? J. Med. Nucl. 54 (2013) 815–824.
[72] D. Vriens, E.P. Visser, L.-F. de Geus-Oei, W.J. Oyen, Methodological considerations in quantification of oncological FDG PET studies, Eur. J. Nucl. Med. Mol. Imaging 37 (2010) 1408–1425.
[73] C.F. Baumgartner, C. Kolbitsch, D.R. Balfour, P.K. Marsden, J.R. McClelland, D. Rueckert, A.P. King, High-resolution dynamic MR imaging of the thorax for respiratory motion correction of PET using groupwise manifold alignment, Med. Image Anal. 18 (2014) 939–952.
[74] H. Fayad, F. Monnier, F. Odille, J. Felblinger, F. Lamare, D. Visvikis, Respiratory and cardiac motion correction in dual gated PET/MR imaging, EJNMMI Phys. 2 (2015) A43.

[75] A. Martinez-Möller, S.G. Nekolla, Attenuation correction for PET/MR: problems, novel approaches and practical solutions, Z. Med. Phys. 22 (2012) 299–310.
[76] V. Keereman, P. Mollet, Y. Berker, V. Schulz, S. Vandenberghe, Challenges and current methods for attenuation correction in PET/MR, Magn. Reson. Mater. Phys. 26 (2013) 81–98.
[77] J. Gaa, E.J. Rummeny, M.D. Seemann, Whole-body imaging with PET/MRI, Eur. J. Med. Res. 9 (2004) 309–312.
[78] A.M. Ho, B.N. Kalantari, PET/MRI: a new frontier in breast cancer imaging, Breast J. 22 (2016) 261–263.
[79] C. Brendle, N.F. Schwenzer, H. Rempp, H. Schmidt, C. Pfannenberg, C. la Fougère, K. Nikolaou, C. Schraml, Assessment of metastatic colorectal cancer with hybrid imaging: comparison of reading performance using different combinations of anatomical and functional imaging techniques in PET/MRI and PET/CT in a short case series, Eur. J. Nucl. Med. Mol. Imaging 43 (2016) 123–132.
[80] A. Ciarmiello, L. Mansi, I. Carrio, PET/CT versus PET/MRI, in: A. Ciarmiello, L. Mansi (Eds.), PET-CT and PET-MRI in Neurology: SWOT Analysis Applied to Hybrid Imaging, Springer International Publishing, Cham, 2016, , pp. 297–310.
[81] I. Binse, T.D. Poeppel, M. Ruhlmann, B. Gomez, L. Umutlu, A. Bockisch, S. J. Rosenbaum-Krumme, Imaging with 124I in differentiated thyroid carcinoma: is PET/MRI superior to PET/CT? Eur. J. Nucl. Med. Mol. Imaging 43 (2016) 1011–1017.
[82] A. Sabet, J. Cohnen, K. Beiderwellen, S. Ezziddin, L. Umutlu, A. Bellendorf, H. Grafe, F. Nensa, A. Bockisch, T. Poeppel, Simultaneous 68Ga-DOTATOC-PET/MRI for characterization of undetermined upper abdominal tracer uptake in 68Ga-DOTATOC PET/CT, J. Nucl. Med. 57 (2016) 1595.
[83] R. Madru, T.A. Tran, J. Axelsson, C. Ingvar, A. Bibic, F. Ståhlberg, L. Knutsson, S.-E. Strand, 68Ga-labeled superparamagnetic iron oxide nanoparticles (SPIONs) for multi-modality PET/MR/Cherenkov luminescence imaging of sentinel lymph nodes, Am. J. Nucl. Med. Mol. Imaging 4 (2014) 60–69.
[84] A. Lahooti, S. Sarkar, H. Saligheh Rad, A. Gholami, S. Nosrati, R.N. Muller, S. Laurent, C. Grüttner, P. Geramifar, H. Yousefnia, M. Mazidi, S. Shanehsazzadeh, PEGylated superparamagnetic iron oxide nanoparticles labeled with 68Ga as a PET/MRI contrast agent: a biodistribution study, J. Radioanal. Nucl. Chem. 311 (1) (2017) 769–774.
[85] X. Huang, F. Zhang, S. Lee, M. Swierczewska, D.O. Kiesewetter, L. Lang, G. Zhang, L. Zhu, H. Gao, H.S. Choi, Long-term multimodal imaging of tumor draining sentinel lymph nodes using mesoporous silica-based nanoprobes, Biomaterials 33 (2012) 4370–4378.
[86] C. Truillet, P. Bouziotis, C. Tsoukalas, J. Brugière, M. Martini, L. Sancey, T. Brichart, F. Denat, F. Boschetti, U. Darbost, Ultrasmall particles for Gd-MRI and 68Ga-PET dual imaging, Contrast Media Mol. Imaging 10 (4) (2015) 309–319.
[87] L. Stelter, J. Pinkernelle, R. Michel, R. Schwartländer, N. Raschzok, M. Morgul, M. Koch, T. Denecke, J. Ruf, H. Bäumler, A. Jordan, B. Hamm, I. Sauer, U. Teichgräber, Modification of aminosilanized superparamagnetic nanoparticles: feasibility of multimodal detection using 3 T MRI, small animal PET, and fluorescence imaging, Mol. Imaging Biol. 12 (2010) 25–34.
[88] S.-m. Kim, M.K. Chae, M.S. Yim, I.H. Jeong, J. Cho, C. Lee, E.K. Ryu, Hybrid PET/MR imaging of tumors using an oleanolic acid-conjugated nanoparticle, Biomaterials 34 (2013) 8114–8121.
[89] B.Y. Yang, S.-H. Moon, S.R. Seelam, M.J. Jeon, Y.-S. Lee, D.S. Lee, J.-K. Chung, Y.I. Kim, J.M. Jeong, Development of a multimodal imaging probe by encapsulating iron oxide nanoparticles with functionalized amphiphiles for lymph node imaging, Nanomedicine 10 (2015) 1899–1910.

[90] E. Locatelli, L. Gil, L.L. Israel, L. Passoni, M. Naddaka, A. Pucci, T. Reese, V. Gomez-Vallejo, P. Milani, M. Matteoli, J. Llop, J.P. Lellouche, M.C. Franchini, Biocompatible nanocomposite for PET/MRI hybrid imaging, Int. J. Nanomed. 7 (2012) 6021–6033.
[91] S.-H. Moon, B.Y. Yang, Y.J. Kim, M.K. Hong, Y.-S. Lee, D.S. Lee, J.-K. Chung, J. M. Jeong, Development of a complementary PET/MR dual-modal imaging probe for targeting prostate-specific membrane antigen (PSMA), Nanomedicine 12 (4) (2016) 871–879.
[92] X. Yang, H. Hong, J.J. Grailer, I.J. Rowland, A. Javadi, S.A. Hurley, Y. Xiao, Y. Yang, Y. Zhang, R.J. Nickles, cRGD-functionalized, DOX-conjugated, and 64 Cu-labeled superparamagnetic iron oxide nanoparticles for targeted anticancer drug delivery and PET/MR imaging, Biomaterials 32 (2011) 4151–4160.
[93] H.-Y. Lee, Z. Li, K. Chen, A.R. Hsu, C. Xu, J. Xie, S. Sun, X. Chen, PET/MRI dual-modality tumor imaging using arginine-glycine-aspartic (RGD)-conjugated radiolabeled iron oxide nanoparticles, J. Nucl. Med. 49 (2008) 1371–1379.
[94] R. Torres Martin de Rosales, R. Tavaré, R.L. Paul, M. Jauregui-Osoro, A. Protti, A. Glaria, G. Varma, I. Szanda, P.J. Blower, Synthesis of 64CuII–bis (dithiocarbamatebisphosphonate) and its conjugation with superparamagnetic iron oxide nanoparticles: in vivo evaluation as dual-modality PET–MRI agent, Angew. Chem. Int. Ed. Engl. 50 (2011) 5509–5513.
[95] C. Glaus, R. Rossin, M.J. Welch, G. Bao, In vivo evaluation of 64Cu-labeled magnetic nanoparticles as a dual-modality PET/MR imaging agent, Bioconjug. Chem. 21 (2010) 715–722.
[96] T. Liu, S. Shi, C. Liang, S. Shen, L. Cheng, C. Wang, X. Song, S. Goel, T.E. Barnhart, W. Cai, Iron oxide decorated MoS2 nanosheets with double PEGylation for chelator-free radiolabeling and multimodal imaging guided photothermal therapy, ACS Nano 9 (1) (2015) 950–960.
[97] H. Zhang, 64Cu-DTPA-CLIO-VT680, in: Molecular Imaging and Contrast Agent Database (MICAD), National Center for Biotechnology Information, Bethesda, MD, 2004.
[98] X. Cui, S. Belo, D. Krüger, Y. Yan, R.T. de Rosales, M. Jauregui-Osoro, H. Ye, S. Su, D. Mathe, N. Kovács, Aluminium hydroxide stabilised $MnFe_2O_4$ and Fe_3O_4 nanoparticles as dual-modality contrasts agent for MRI and PET imaging, Biomaterials 35 (2014) 5840–5846.
[99] J. Xie, K. Chen, J. Huang, S. Lee, J. Wang, J. Gao, X. Li, X. Chen, PET/NIRF/MRI triple functional iron oxide nanoparticles, Biomaterials 31 (2010) 3016–3022.
[100] X. Lin, J. Xie, G. Niu, F. Zhang, H. Gao, M. Yang, Q. Quan, M.A. Aronova, G. Zhang, S. Lee, R. Leapman, X. Chen, Chimeric ferritin nanocages for multiple function loading and multimodal imaging, Nano Lett. 11 (2011) 814–819.
[101] H. Hu, D. Li, S. Liu, M. Wang, R. Moats, P.S. Conti, Z. Li, Integrin $\alpha_2\beta_1$ targeted $GdVO_4$:Eu ultrathin nanosheet for multimodal PET/MR imaging, Biomaterials 35 (2014) 8649–8658.
[102] S. Aryal, J. Key, C. Stigliano, M.D. Landis, D.Y. Lee, P. Decuzzi, Positron emitting magnetic nanoconstructs for PET/MR imaging, Small 10 (2014) 2688–2696.
[103] X. Cui, D. Mathe, N. Kovács, I. Horváth, M. Jauregui-Osoro, R. Torres Martin de Rosales, G.E. Mullen, W. Wong, Y. Yan, D. Krüger, Synthesis, characterization, and application of core-shell $Co_{0.16}Fe_{2.84}O_4$@ $NaYF_4$ (Yb, Er) and Fe_3O_4@ $NaYF_4$ (Yb, Tm) nanoparticle as trimodal (MRI, PET/SPECT, and optical) imaging agents, Bioconjug. Chem. 27 (2) (2016) 319–328.
[104] M. Yang, Q. Fan, R. Zhang, K. Cheng, J. Yan, D. Pan, X. Ma, A. Lu, Z. Cheng, Dragon fruit-like biocage as an iron trapping nanoplatform for high efficiency targeted cancer multimodality imaging, Biomaterials 69 (2015) 30–37.

[105] Q. Fan, K. Cheng, X. Hu, X. Ma, R. Zhang, M. Yang, X. Lu, L. Xing, W. Huang, S.S. Gambhir, Transferring biomarker into molecular probe: melanin nanoparticle as a naturally active platform for multimodality imaging, J. Am. Chem. Soc. 136 (2014) 15185–15194.
[106] B.R. Jarrett, C. Correa, K.L. Ma, A.Y. Louie, In vivo mapping of vascular inflammation using multimodal imaging, PLoS One 5 (2010) e13254.
[107] B.R. Jarrett, B. Gustafsson, D.L. Kukis, A.Y. Louie, Synthesis of (64)Cu-labeled magnetic nanoparticles for multimodal imaging, Bioconjug. Chem. 19 (2008) 1496–1504.
[108] M. Nahrendorf, E. Keliher, B. Marinelli, F. Leuschner, C.S. Robins, R.E. Gerszten, M.J. Pittet, F.K. Swirski, R. Weissleder, Detection of macrophages in aortic aneurysms by nanoparticle PET-CT, Arterioscler. Thromb. Vasc. Biol. 31 (2011) 750–757.
[109] R. Sharma, Y. Xu, S.W. Kim, M.J. Schueller, D. Alexoff, S.D. Smith, W. Wang, D. Schlyer, Carbon-11 radiolabeling of iron-oxide nanoparticles for dual-modality PET/MR imaging, Nanoscale 5 (2013) 7476–7483.
[110] J.s. Choi, J.C. Park, H. Nah, S. Woo, J. Oh, K.M. Kim, G.J. Cheon, Y. Chang, J. Yoo, J. Cheon, A hybrid nanoparticle probe for dual-modality positron emission tomography and magnetic resonance imaging, Angew. Chem. Int. Ed. Engl. 47 (2008) 6259–6262.
[111] J. Lee, T.S. Lee, J. Ryu, S. Hong, M. Kang, K. Im, J.H. Kang, S.M. Lim, S. Park, R. Song, RGD peptide-conjugated multimodal $NaGdF_4$:Yb^{3+}/Er^{3+} nanophosphors for upconversion luminescence, MR, and PET imaging of tumor angiogenesis, J. Nucl. Med. 54 (2013) 96–103.
[112] J.C. Park, M.K. Yu, G.I. An, S.I. Park, J. Oh, H.J. Kim, J.H. Kim, E.K. Wang, I.H. Hong, Y.S. Ha, T.H. Choi, K.S. Jeong, Y. Chang, M.J. Welch, S. Jon, J. Yoo, Facile preparation of a hybrid nanoprobe for triple-modality optical/PET/MR imaging, Small 6 (2010) 2863–2868.
[113] R. Chakravarty, H.F. Valdovinos, F. Chen, C.M. Lewis, P.A. Ellison, H. Luo, M.E. Meyerand, R.J. Nickles, W. Cai, Intrinsically germanium-69-labeled iron oxide nanoparticles: synthesis and in-vivo dual-modality PET/MR imaging, Adv. Mater. 26 (2014) 5119–5123.
[114] R. Torres Martin de Rosales, R. Tavaré, A. Glaria, G. Varma, A. Protti, P.J. Blower, 99mTc-bisphosphonate-iron oxide nanoparticle conjugates for dual-modality biomedical imaging, Bioconjug. Chem. 22 (2011) 455–465.
[115] C.M. Lee, H.J. Jeong, E.M. Kim, D.W. Kim, S.T. Lim, H.T. Kim, I.K. Park, Y.Y. Jeong, J.W. Kim, M.H. Sohn, Superparamagnetic iron oxide nanoparticles as a dual imaging probe for targeting hepatocytes in vivo, Magn. Reson. Med. 62 (2009) 1440–1446.
[116] I. Tsiapa, E.K. Efthimiadou, E. Fragogeorgi, G. Loudos, A.D. Varvarigou, P. Bouziotis, G.C. Kordas, D. Mihailidis, G.C. Nikiforidis, S. Xanthopoulos, 99 m Tc-labeled aminosilane-coated iron oxide nanoparticles for molecular imaging of $\alpha v\beta_3$-mediated tumor expression and feasibility for hyperthermia treatment, J. Colloid Interface Sci. 433 (2014) 163–175.
[117] R. Madru, P. Kjellman, F. Olsson, K. Wingårdh, C. Ingvar, F. Ståhlberg, J. Olsrud, J. Lätt, S. Fredriksson, L. Knutsson, 99mTc-labeled superparamagnetic iron oxide nanoparticles for multimodality SPECT/MRI of sentinel lymph nodes, J. Nucl. Med. 53 (2012) 459–463.
[118] S. Shanehsazzadeh, A. Lahooti, Biodistribution of 80 nm iron oxide nanoparticles labeled with 99mTc in Balb/c mice, Nucl. Med. Biol. 7 (2014) 625.
[119] S. Shanehsazzadeh, M.A. Oghabian, F.J. Daha, M. Amanlou, B.J. Allen, Biodistribution of ultra small superparamagnetic iron oxide nanoparticles in BALB mice, J. Radioanal. Nucl. Chem. 295 (2013) 1517–1523.

[120] S. Shanehsazzadeh, C. Gruettner, A. Lahooti, M. Mahmoudi, B.J. Allen, M. Ghavami, F.J. Daha, M.A. Oghabian, Monoclonal antibody conjugated magnetic nanoparticles could target MUC-1-positive cells in vitro but not in vivo, Contrast Media Mol. Imaging 10 (2015) 225–236.
[121] H. Wang, R. Kumar, D. Nagesha, R.I. Duclos, S. Sridhar, S.J. Gatley, Integrity of 111 In-radiolabeled superparamagnetic iron oxide nanoparticles in the mouse, Nucl. Med. Biol. 42 (2015) 65–70.
[122] A. Natarajan, C.-Y. Xiong, C. Gruettner, G.L. DeNardo, S.J. DeNardo, Development of multivalent radioimmunonanoparticles for cancer imaging and therapy, Cancer Biother. Radiopharm. 23 (2008) 82–91.
[123] R. Misri, D. Meier, A.C. Yung, P. Kozlowski, U.O. Häfeli, Development and evaluation of a dual-modality (MRI/SPECT) molecular imaging bioprobe, Nanomedicine 8 (2012) 1007–1016.
[124] A. Natarajan, C. Gruettner, R. Ivkov, G.L. DeNardo, G. Mirick, A. Yuan, A. Foreman, S.J. DeNardo, Nanoferrite particle based radioimmunonanoparticles: binding affinity and in vivo pharmacokinetics, Bioconjug. Chem. 19 (2008) 1211–1218.
[125] S. Deng, W. Zhang, B. Zhang, R. Hong, Q. Chen, J. Dong, Y. Chen, Z. Chen, Y. Wu, Radiolabeled cyclic arginine-glycine-aspartic (RGD)-conjugated iron oxide nanoparticles as single-photon emission computed tomography (SPECT) and magnetic resonance imaging (MRI) dual-modality agents for imaging of breast cancer, J. Nanopart. Res. 17 (2015) 1–11.
[126] J. Zhu, B. Zhang, J. Tian, J. Wang, Y. Chong, X. Wang, Y. Deng, M. Tang, Y. Li, C. Ge, Synthesis of heterodimer radionuclide nanoparticles for magnetic resonance and single-photon emission computed tomography dual-modality imaging, Nanoscale 7 (8) (2015) 3392–3395.
[127] D. Hoffman, M. Sun, L. Yang, P.R. McDonagh, F. Corwin, G. Sundaresan, L. Wang, V. Vijayaragavan, C. Thadigiri, N. Lamichhane, Intrinsically radiolabelled [59Fe]-SPIONs for dual MRI/radionuclide detection, Am. J. Nucl. Med. Mol. Imaging 4 (6) (2014) 548–560.
[128] D.L. Thorek, D. Ulmert, N.-F.M. Diop, M.E. Lupu, M.G. Doran, R. Huang, D.S. Abou, S.M. Larson, J. Grimm, Non-invasive mapping of deep-tissue lymph nodes in live animals using a multimodal PET/MRI nanoparticle, Nat. Commun. 5 (2014) 3097.
[129] H.Y. Ko, J.H. Lee, H. Kang, S.H. Ryu, I.C. Song, D.S. Lee, S. Kim, A nucleolin-targeted multimodal nanoparticle imaging probe for tracking cancer cells using an aptamer, J. Nucl. Med. 51 (2010) 98–105.
[130] S. Shanehsazzadeh, M.A. Oghabian, A. Lahooti, M. Abdollahi, S.A. Haeri, M. Amanlou, F.J. Daha, B.J. Allen, Estimated background doses of [67Ga]-DTPA-USPIO in normal Balb/c mice as a potential therapeutic agent for liver and spleen cancers, Nucl. Med. Commun. 34 (2013) 915–925.
[131] S. Nosrati, S. Shanehsazzadeh, H. Yousefnia, A. Gholami, C. Grüttner, A. Jalilian, R. Hosseini, A. Lahooti, Biodistribution evaluation of 166Ho-DTPA-SPION in normal rats, J. Radioanal. Nucl. Chem. 307 (2) (2016) 1559–1566.